Large Currents Generate Cardiac Ca^{2+} Sparks

Leighton T. Izu,* Joseph R. H. Mauban,[†] C. W. Balke,*[†] and W. Gil Wier*[†]
Departments of *Medicine and [†]Physiology, University of Maryland, Baltimore, Baltimore, Maryland 21201, USA

ABSTRACT   Previous models of cardiac Ca^{2+} sparks have assumed that Ca^{2+} currents through the Ca^{2+} release units (CRUs) were ~1–2 pA, producing sparks with peak fluorescence ratio (F/F_0) of ~2.0 and a full-width at half maximum (FWHM) of ~1 μm. Here, we present actual Ca^{2+} sparks with peak F/F_0 of >6 and a FWHM of ~2 μm, and a mathematical model of such sparks, the main feature of which is a much larger underlying Ca^{2+} current. Assuming infinite reaction rates and no endogenous buffers, we obtain a lower bound of ~11 pA needed to generate a Ca^{2+} spark with FWHM of 2 μm. Under realistic conditions, the CRU current must be ~20 pA to generate a 2-μm Ca^{2+} spark. For currents $\geq$5 pA, the computed spark amplitudes (F/F_0) are large (~6–12 depending on buffer model). We considered several factors that might produce sparks with FWHM ~ 2 μm without using large currents. Possible protein–dye interactions increased the FWHM slightly. Hypothetical Ca^{2+} "quarks" had little effect, as did blurring of sparks by the confocal microscope. A clusters of CRUs, each producing 10 pA simultaneously, can produce sparks with FWHM ~ 2 μm. We conclude that cardiac Ca^{2+} sparks are significantly larger in peak amplitude than previously thought, that such large Ca^{2+} sparks are consistent with the measured FWHM of ~2 μm, and that the underlying Ca^{2+} current is in the range of 10–20 pA.

GLOSSARY

x, y, z = space coordinates (μm)

t = time coordinate (ms)

C = free cytosolic Ca^{2+} concentration (μM)

F_D = free fluo-3 concentration (μM)

G_D = Ca-bound fluo-3 concentration

H_D = total fluo-3 concentration ($F_D + G_D$)

F_B = free endogenous buffer concentration (μM)

G_B = Ca-bound endogenous buffer concentration (μM)

H_B = total endogenous buffer concentration (μM)

D_{Cs}, D_{Cy}, D_{Cz} = Ca^{2+} diffusion coefficients along x, y, and z directions (μm^2/ms)

D_{Dx}, D_{Dy}, D_{Dz} = fluo-3 diffusion coefficients of both free and Ca-bound forms

I_{SR} = current through Ca^{2+} release unit (pA)

T_{open} = open time of Ca^{2+} release unit (ms)

J_{SR} = molar flux of Ca^{2+} through Ca^{2+} release unit (pmol/ms)

J_P = SR-ATPase pump rate (μM/ms)

V_P = maximum SR pump rate (μM/ms)

K_P = SR pump Michaelis constant (μM)

n_p = SR pump Hill coefficient

J_{leak} = Ca^{2+} leak rate through SR (μM/ms)

k_j^+, k_j^- = forward and reverse rate constants for buffer reactions ($j = D$ for dye, $j = B$ for endogenous buffer)

$\lambda_x, \lambda_y, \lambda_z$ = full-width at half-maximum (FWHM) of G_D along x, y, z (μm)

C_o = resting Ca^{2+} concentration (μM)

INTRODUCTION

Current mathematical models of cardiac Ca^{2+} sparks (Smith et al., 1998; Izu et al., 1998) are deficient in several respects. First, most models replicate the amplitude of the average confocally recorded Ca^{2+} spark [typical peak fluorescence ratio (F/F_0) of 2], yet, such a spark most likely represents an "out-of-focus" event whose peak amplitude may be several times less than that of an "in-focus" Ca^{2+} spark. Recently, we recorded Ca^{2+} sparks of peak F/F_0 of up to 6.0, larger than any reported previously (Wier et al., 2000). Currents required to generate such large Ca^{2+} sparks could be much larger than previously assumed, with important implications for the molecular mechanisms of cardiac Ca^{2+} sparks. Second, all mathematical models fail by a large margin to reproduce the spatial characteristics of recorded Ca^{2+} sparks, both cardiac (Smith et al., 1998; Izu et al., 1998) and skeletal (Jiang et al., 1999). The fluorescence distribution in model cardiac Ca^{2+} sparks is typically spherically symmetrical, and Gaussian in profile with a full-width at half maximum (FWHM) of about 1.0 μm. Although recorded Ca^{2+} sparks are indeed Gaussian in profile, they are often not spherically symmetrical (Parker et al., 1996; Cheng et al., 1996b) and both cardiac and skeletal Ca^{2+} sparks typically have an FWHM in the longitudinal direction (i.e., along the long cell axis) of about 2.0 μm. The possible significance of this deficiency of model cardiac Ca^{2+} sparks was made apparent to us when we were unable to model satisfactorily the evolution of cardiac Ca^{2+} waves from stochastically occurring Ca^{2+} sparks (Izu et al., 1999). We hypothesized that this attempt failed in part because the properties of the model cardiac Ca^{2+} sparks were not correct. Previous, deterministic, one-dimensional models of Ca^{2+} waves (Backx et al., 1989) would not have encountered this difficulty, but should now be regarded as unreal-

istic, because the experimental evidence is that cardiac Ca^{2+} waves arise from sequential activation of Ca^{2+} sparks (Cheng et al., 1996a; Wier et al., 1997; Lukyanenko et al., 1999). The present study was undertaken to remedy these deficiencies by verifying the existence of Ca^{2+} sparks of such large amplitude in mammalian cardiac muscle and by producing a model of cardiac Ca^{2+} sparks that matched the spatial properties and their peak amplitude.

METHODS

Preparation of cells and recording of Ca²⁺ sparks

Two-month-old Sprague-Dawley rats (body weight, 180–280 g) were heparinized (10 iu g⁻¹ i.p.) and anesthetized with sodium pentobarbital (170 mg kg⁻¹ injected i.p.). The heart was removed while still beating by means of a mid-line thoracotomy. Single ventricular cells were obtained by an enzymatic dispersion technique described previously (López-López et al., 1995). Cells were loaded with the acetoxymethyl ester form of fluo-3 or fluo-4 using a dye stock solution consisting of 50 μg of dye in 40 μl of DMSO. Pluronic (25% w/v in DMSO), 1.5 μl, was added (this solution was vortexed). Ten microliters of this solution was added to 500 μl of the physiological salt solution (see below) containing the cells. This solution was kept in the dark for 30 min and mixed gently. Cells were placed in a rotatable chamber so that they could be aligned for confocal scanning, parallel to their long axis (x axis). Recordings were made at room temperature, with cells bathed in a physiological salt solution containing (composition in mM): NaCl, 140; dextrose, 10; HEPES, 10; KCl, 4.0; MgCl₂, 1; CaCl₂, 1; pH adjusted to 7.3–7.4 with NaOH. The performance (spatial resolution and dynamic range) of the confocal microscope used for recording Ca^{2+} sparks has been described in detail recently (Wier et al., 2000). With the 63X 1.4 NA oil immersion objective used in the present study, the resolution of the confocal system is 0.25 μm (laterally) and 0.52 μm (axially). Line-scan images were typically 256 pixels per line, at 0.1 μm per pixel, and 512 lines per frame, at 3.0 ms per line. The relatively small pixel size ensures that the Nyquist criterion is met, because the FWHM of the point spread function (PSF) of the microscope is 0.25 μm. Pixels are typically 10.0 μs in duration, giving time for linear scanning of 2.560 ms, with 440 μs for mirror "flyback." The number of counts per pixel typically did not exceed 50, corresponding to a count rate of 5×10^6 cps, with a pixel duration of 10.0 μs.

Mathematical modeling of Ca²⁺ binding and diffusion

The reactions we consider are those of Ca^{2+} (C) with the free endogenous Ca^{2+}-buffer molecules (F_B) and with the free fluorescent indicator dye, fluo-3 (F_D). We assume simple one-to-one binding reactions, given as

$$F_B + C \leftrightarrow G_B = H_B - F_B,$$

$$F_D + C \leftrightarrow G_D = H_D - F_D.$$

The forward and reverse kinetic constants are k_j^+ and k_j^- where j is either B or D. G_j denotes the concentration of the Ca^{2+}-bound species and H_j is the total concentration (bound + unbound). Ca^{2+}, free dye, and Ca^{2+}-bound dye (G_D) are assumed to be mobile, with the latter two having the same diffusion coefficient. Free endogenous buffer and Ca^{2+}-bound endogenous buffer (G_B) are assumed to be immobile. Including terms for

release and leak of Ca^{2+} from the sarcoplasmic reticulum (SR) and active transport of Ca^{2+} into the SR (see below), the reaction–diffusion equations are then

$$\frac{\partial C}{\partial t} = \nabla \cdot (D_C \nabla C) + \sum_j R_j(C, F_j, H_j)$$
$$+ J_{SR}\delta(r) - J_p + J_{leak}, \tag{1}$$

$$\frac{\partial F_D}{\partial t} = \nabla \cdot (D_D \nabla F_D) + R_D(C, F_D, H_D), \tag{2}$$

$$\frac{\partial F_B}{\partial t} = R_B(C, F_B, H_B), \tag{3}$$

where

$$R_j(C, F_j, H_j) = -k_j^+ C \cdot F_j + k_j^- (H_j - F_j) \tag{4}$$

is the net rate of the bimolecular reaction and

$$H_j = F_j + G_j, \tag{5}$$

where $j = D$ or B.

Depending on our purpose, we will assume either that diffusion is spherically symmetric or anisotropic. For spherically symmetric diffusion, $\nabla \cdot (D_C \nabla C)$ is $D_C(\partial^2 C/\partial r^2 + (2/r)\partial C/\partial r)$ (Crank, 1975), and for anisotropic diffusion, it is given by

$$\nabla \cdot (D_C \nabla C) = D_{Cx} \frac{\partial^2 C}{\partial x^2} + D_{Cy} \frac{\partial^2 C}{\partial y^2} + D_{Cz} \frac{\partial^2 C}{\partial z^2}. \tag{6}$$

Note that we are assuming that the principal diffusion axes coincide with the axes of the cell. The x-axis of the cell is the long axis, the y-axis is transverse to the long axis, and the z-axis coincides with the microscope's optical axis. Since the transverse and axial directions appear similar in cardiac cells, we will always assume that $D_{Cy} = D_{Cz}$.

$J_{SR}\delta(r)$ is the point source of Ca^{2+} release from the SR, located at the origin, and $\delta(r)$ is the Dirac delta-function. Following Franzini-Armstrong et al. (1999), we call the Ca^{2+} source the Ca^{2+} release unit (CRU). J_{SR} is related to the CRU current I_{SR} by $J_{SR} = I_{SR}/(zF)$, where $z = 2$ and F is Faraday's constant. J_p represents Ca^{2+} pumping by the SR-ATPase and is

$$J_p = \frac{V_p C^{n_p}}{K^{n_p} + C^{n_p}}, \tag{7}$$

where $V_p = 200$ μM/s, $K_p = 184$ nM, and $n_p = 4$ (Balke et al., 1994). J_{leak} is the Ca^{2+} leak from the SR and is adjusted so that, at the resting Ca^{2+} concentration (100 nM), $J_{leak} - J_p = 0$.

A substantial amount of fluorescent indicator can be bound to proteins (Blatter and Wier, 1990; Harkins et al., 1993) that immobilize the dye. In a previous paper (Izu et al., 1998), we included the reaction of Ca^{2+} with the protein-bound indicator. This time, to reduce the computational load, we take the approach of Smith et al. (1998) and eliminate the protein-bound indicator reaction with Ca^{2+}. Smith et al. (1998) compensate for the elimination of the dye immobilizing reaction by reducing the diffusion coefficient of the indicator from the calculated value (from Stoke's law) of 0.09 to 0.02 μm²/ms. The rate constants for the reaction of Ca^{2+} with fluo-3, $k_D^+ = 80/\mu$M/s and $k_D^- = 90$/s, are from Smith et al. (1998). We will refer to the set of reactions given in Eqs. 1–5 and the set of rate constants and diffusivities just given as the "Smith buffer model" to distinguish them from another set of reactions, which we describe later. Simulation parameters for the Smith buffer model are given in Table 1. The simulations always start with all chemical species in chemical equilibrium and no gradients. Thus a conservation relationship exists between G_j, F_j, and H_j,

TABLE 1   Standard parameter values for Smith buffer model

Parameter	Value
F_D	50 μM
H_B	123 μM*
D_{Cx}, D_{Cy}, D_{Cz}	0.3, 0.15, 0.15 μm²/ms[†‡]
D_{Dx}, D_{Dy}, D_{Dz}	0.02, 0.01, 0.01 μm²/ms[§]
T_{open}	5 ms[¶‖]
V_P	200 μM/s**
K_P	0.184 μM**
n_P	4**
k_B^+, k_B^-	100/μM/s, 100/s*
k_D^+, k_D^-	80/μM/s, 90/s[§]
C_o	0.1 μM

*Berlin et al., 1994.
[†]Baylor and Hollingworth, 1998.
[‡]For spherically symmetric case, diffusion coefficients along y and z are the same as along x.
[§]Smith et al., 1998.
[¶]Rousseau and Meissner, 1989.
[‖]Lacampagne et al., 1999.
**Balke et al., 1994.

and there is no differential equation for G_j. Zero-flux boundary conditions were imposed in all cases.

Numerical solution of the reaction-diffusion equations

The model equations were solved numerically by Facsimile (AEA Technologies, Harwell, UK), using the method of lines. The spatial derivatives were approximated by center differences. Accuracy of the codes (spherically symmetric and anisotropic models) were checked by eliminating all reactions and comparing simulation results with the analytic solution (see Appendix C). In both cases, the simulation agreed with the analytic solution to a few percent for distances >0.1 μm. To check the accuracy of the solution in the spherically symmetric case when nonlinear reactions were present, we halved the step size and found the solutions to be virtually identical to the solution with the 0.01-μm step size. Such high resolution was not possible (because of computer memory limitations) for the anisotropic case. For this case, the spatial step size (equal in all three directions) was either 0.05 or 0.1 μm. The domain length was 6 μm for the spherically symmetric case and either 2 or 3 μm for the anisotropic case. In all cases, we checked to ensure that C, F_B, and F_D at the boundaries were within 0.1% of their resting values.

Simulating blurring by the microscope

To simulate optical blurring of the spark by the microscope, we convolved the 3-dimensional (3D) distribution of Ca²⁺-bound indicator, G_D, with a Gaussian kernel that approximates the PSF of a microscope (Izu et al., 1998). This was done by first multiplying the discrete Fourier transform (DFT) of G_D with the DFT of the PSF and then performing the inverse transform. The size of the DFTs were 128 × 128 × 128, corresponding to a spatial length of 3 μm in all directions. The standard PSF had an FWHM of (fwhm$_x$, fwhm$_y$, fwhm$_z$) = (0.4 μm, 0.4 μm, 0.8 μm).

RESULTS

Ca²⁺ sparks

A histogram of the peak amplitudes (F/F_0) of a large number of Ca²⁺ sparks from 21 cells from one animal is pre-

sented in Fig. 1 *A*. The FWHM of these sparks is presented in Fig. 1 *B*. All recordings were made with scanning along the longitudinal or *x* axis of the cell. Similar results were obtained in a total of 6 animals. In all cases, large numbers of Ca²⁺ sparks were recorded with peak amplitudes greater than 4.0, and ranging, in some cases, up to 9.0. The distribution of amplitudes conforms roughly to the inverse hyperbolic form predicted from the theory of confocal sampling (Izu et al., 1998). Except in rat atrial cells (Blatter et al., 1997), we are not aware of any previous studies in which Ca²⁺ sparks greater than 4.0 have been recorded in cardiac tissue. For example, the maximum F/F_0 reported in a recent study of a large number of cardiac Ca²⁺ sparks was less than 3.0 (Cheng et al., 1999). The Ca²⁺ sparks illustrated in Fig. 1 were detected "by eye," rather than by an automatic detection system. Thus, the amplitude distribution is distorted at the low end, due to the inability of a human observer to distinguish small Ca²⁺ sparks from noise. Spark detection by the observer has no effect on the upper end of the distribution. We attribute the detection of large Ca²⁺ sparks primarily to the use of a confocal microscope with high spatial resolution (Wier et al., 2000). The modal value of the distribution of FWHM was ~2 μm. The largest Ca²⁺ sparks, with which we are concerned here, typically had FWHM of ~2 μm and were Gaussian in profile, as shown in Fig. 1 *D*.

Modeling the cardiac Ca²⁺ spark

Equilibrium, Gaussian distribution model

Our objective is to calculate the current through the CRU that is required to produce a spark of a given FWHM in the longitudinal (λ_x), transverse (λ_y), and axial (λ_z) directions. A schematic representation of a spark with these dimensions is shown in Fig. 3, *inset*. The initial calculations will be done with the assumption that calcium binds only to the indicator dye, that C and F_D are always in chemical equilibrium, and that the spatial distribution of Ca²⁺-bound dye, G_D, (hence fluorescence) is Gaussian in all spatial dimensions, at all times. We first present an analytic mathematical proof that, under these conditions, the current found to generate a spark of a given FWHM is the absolute minimum current; the addition of any other specific conditions, such as the inclusion of other Ca²⁺ buffers, and realistic (finite) reaction kinetics will only increase the current required to produce the spark. This is true, as long as none of the chosen conditions violates the assumption of a Gaussian distribution of Ca²⁺-bound dye. The results of the equilibrium analysis will show that even the absolute minimal currents required to produce sparks with an FWHM of ~2.0 μm are substantially larger than previously estimated.

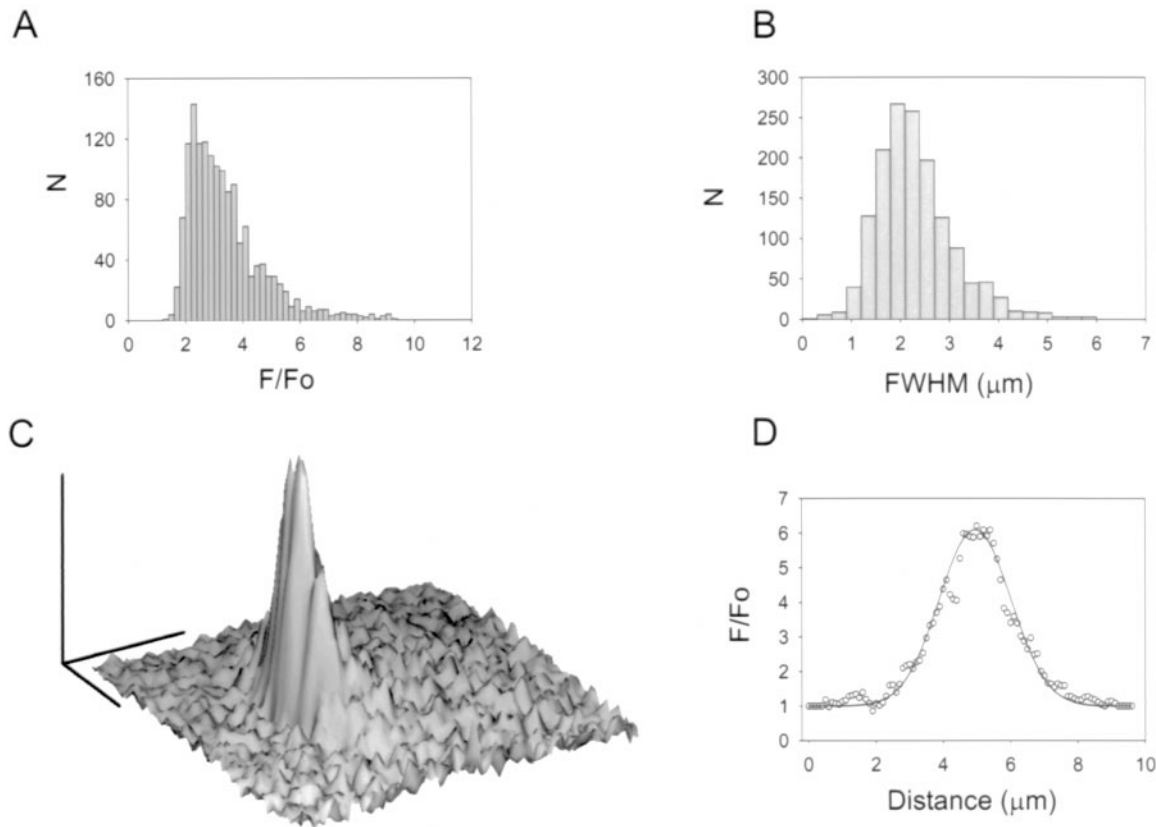FIGURE 1   Large Ca^{2+} sparks in rat ventricular cell. (A) Ca^{2+} spark amplitude histogram. (B) Corresponding values of full-width-half-maximum (FWHM). (C) Shade-surface representation of a typical large Ca^{2+} spark, with peak $F/F_0 > 6.0$. Calibration bars are: x, 2.5 μm; y, 100 ms; z, F/F_0 from 1.0 to 5.0. (D) Spatial profile of spark in (C). FWHM is 2.0 μm, solid line is a Gaussian distribution fit to the data (*open circles*).

Analytical proof of minimum current hypothesis

Let $G_D(x, y, z)$ be the Ca-bound dye concentration and assume it has a Gaussian distribution

$$G_D(x, y, z)$$

$$= G_D^p \exp\left(-\frac{x^2}{(2\sigma_x^2)}\right) \cdot \exp\left(-\frac{y^2}{(2\sigma_y^2)}\right) \cdot \exp\left(-\frac{z^2}{(2\sigma_z^2)}\right). \quad (8)$$

The reason for choosing a Gaussian idealization of the Ca-bound dye concentration is that experimentally measured sparks (Fig. 1 C) and simulated sparks (shown in Fig. 5 A) can be well fit to a Gaussian distribution. The FWHM, λ, is related to σ by $\lambda = \sigma\sqrt{8\ln(2)}$. Let G_D^∞ be the distribution assuming infinite kinetic rates (i.e., all reactions are in equilibrium). We make the important assumption, the validity of which we will examine more closely later, that

$$G_D^\infty(x, y, z) \geq G_D(x, y, z), \quad \text{for all } x, y, z. \quad (9)$$

We prove in Appendix A that G_D^∞ has a larger FWHM than G_D. In other words, the FWHM of the spark generated assuming infinite kinetic rates is larger than the spark generated otherwise. This is important because the current

needed to produce a spark of a given amplitude and spatial size calculated using the equilibrium assumption is a lower bound provided the spark profile is Gaussian.

Now we examine the assumption that $G_D^\infty \geq G_D$ for all x, y, and z. Certainly, at the spark origin $G_D^\infty(0, 0, 0) \geq G_D(0, 0, 0)$, as long as the channel remains open. By continuity, there is a region around the origin where the inequality holds. Away from the origin, the inequality need not hold for all times. Figure 2, A–B, shows the spatial distribution of G_D from simulations in which the Ca–Dye reaction rate was at standard values (*dashed line*) and when the rates were multiplied by 100 (*solid line*), to approximate infinite reaction rates. Figure 2, A and B, shows G_D at 1 and 5 ms after the channel has opened, respectively. The difference between the two (*dotted line*) is nonnegative everywhere. In this case, where the dissociation constant was $K_D = 1.125$ μM, G_D using almost infinite kinetics, $G_D(\sim\infty)$, is everywhere larger than the G_D obtained for moderate kinetic rates, G_D(moderate). When K_D was halved, there is a small region near the base of the spike (about 0.5 μm) where $G_D(\sim\infty)$ is less than G_D(moderate) immediately after the channel opens. For times >2 ms,
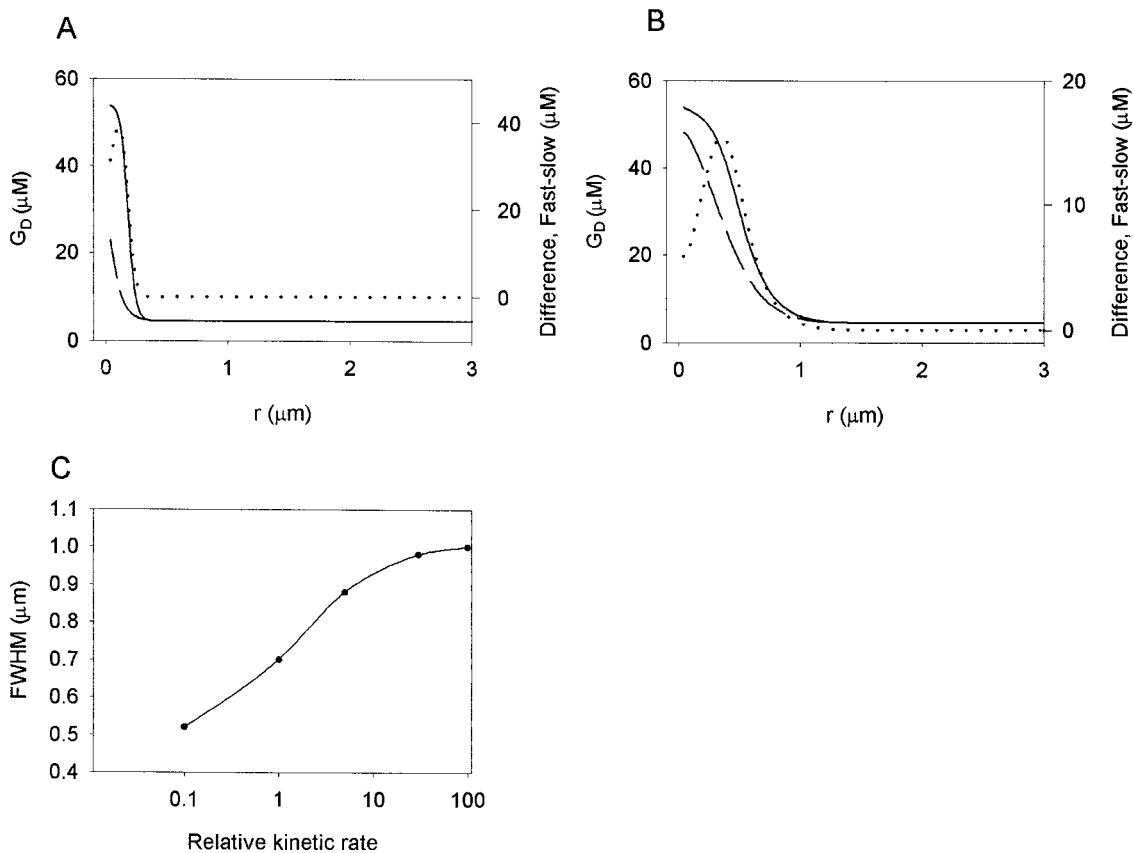
FIGURE 2   Comparison of spatial distribution of Ca-bound dye for very fast and standard kinetics. G_D was numerically computed using the Smith buffer model with the Ca–dye reaction kinetics set to their standard values (*dashed line*) or multiplied by 100 (*solid line*) to approximate an infinitely fast reaction. Panels *A* and *B* show the distribution 1 and 5 ms, respectively, after the channel opens. The difference (*dotted line*) is everywhere positive at 5 ms, but, just after the channel opens, (1 ms)-fast kinetics distribution is about 0.5% lower than the standard kinetic distribution for $0.33 < r < 0.85$. For times >2 ms, however, the faster kinetic distribution is always greater than the slower distribution. This observation supports the assumption that the equilibrium distribution of G_D is an upper bound for G_D for finite kinetic rates. Panel *C* shows the FWHM increasing with increasing reaction rate. In all cases, $k_D^-/k_D^+ = 1.125$ μM.

however, $G_D(\sim\infty) > G_D(\text{moderate})$ everywhere. Because channel openings are on the order of 5–10 ms, the inequality in Eq. 9 is a valid practical assumption, although it is not strictly true for all times.

Numerical simulations of equilibrium, Gaussian distribution model

Numerical simulations provide a complementary way of showing that the FWHM is largest when equilibrium dynamics is assumed. Simulations have the advantage over the analytic proof in not requiring the assumption of a Gaussian distribution of Ca-bound dye and in not assuming the inequality in Eq. 9. (The shortcoming of numerical simulations is that they sample only a tiny portion of parameter space). We solved Eqs. 1–4 with the assumption of radial symmetry. H_B and H_D were fixed, as were k_B^+, k_B^-, and I_{SR}. We multiplied k_D^+ and k_D^- by α from their standard values. The reaction of dye with Ca^{2+} is speeded up or slowed

down relative to the standard, depending on whether α is greater than or less than unity. Figure 2 *C* shows that the FWHM of the simulated spark increases as the reaction speeds up. The numerical simulations and the analytic proof both show that the spatial extent of the spark grows larger as the reaction rates increase. Thus, the current that is required to produce a spark of a given spatial extent is smallest when equilibrium conditions prevail. Next, we calculate the actual value of that current, given the FWHM of the spark.

The minimum requisite current for a spark of a given FWHM

Assuming all reactions involving Ca^{2+} and buffers (*B* and *F*) are in equilibrium, we can calculate C and G_B from the assumed distribution of G_D. C is

$$C(x, y, z) = \frac{K_D G_D(x, y, z)}{H_D - G_D(x, y, z)} \tag{10}$$

from which we calculate

$$G_B(x, y, z) = \frac{H_B \cdot C(x, y, z)}{C(x, y, z) + K_B}. \quad (11)$$

In these equations, $K_i = k_i^-/k_i^+$, $i = B$ or D. The total concentration of C at any point is $\bar{C} = C + G_B + G_D$ and the total number of moles of C is the integral of $\bar{C}$ over the entire volume

$$n(t = T) = \int_{x=-\infty}^{\infty} \int_{y=-\infty}^{\infty} \int_{z=-\infty}^{\infty} \bar{C}(x, y, z) \, \mathrm{d}x \, \mathrm{d}y \, \mathrm{d}z. \quad (12)$$

G_D^p is the concentration of Ca-bound dye at the peak of the spark, $t = T$. Accordingly, $G_D^p = G_D^0 \times F/F_0$, where F/F_0 is the usual measure of spark amplitude. G_D^0 is the concentration at rest and is given by

$$G_D^0 = \frac{H_D}{C_o + K_D}. \quad (13)$$

Numerical quadrature of Eq. 12 was done using Monte Carlo integration (Kahaner et al., 1988). We now want to find the absolute minimal current to produce a Gaussian-shaped spark of a given spatial size. We do this by setting H_B to zero so all released Ca^{2+} is available for binding to fluorescent indicator and not taken up by endogenous buffers. Figure 3 shows the minimum current required to produce sparks of various spatial sizes and amplitude when initial $F_D = 50$ μM. The lower (*circles*) and upper (*triangles*) curves show the currents for spherically symmetric sparks having FWHM of 1 and 2 μm, respectively. The F/F_0 values that we calculate are for an unblurred spark.
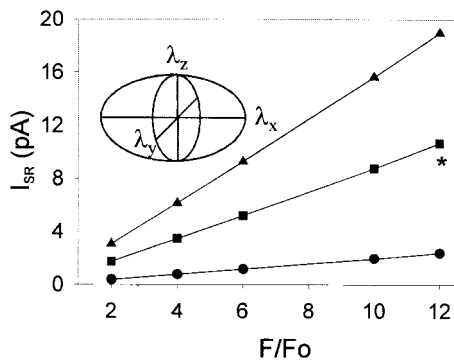

FIGURE 3 Minimum current required to produce a spark of a given spatial size. For these calculations, the fluorescent indicator is the only buffer ($H_B = 0$, $F_D = 50$ μM). Spark dimensions are given by the FWHM (in μm) along the x, y, and z axes, (λ_x, λ_y, λ_z). Inset shows a schematic of an ellipsoidal spark. Note for a spherical spark $\lambda_x = \lambda_y = \lambda_z$. Circles show the current required to produce a spherical spark whose FWHM is 1 μm spark; squares are for an elliptical (2, 1.5, 1.5) spark and triangles are for a spherical (2, 2, 2) spark. The current varies linearly with the spark amplitude F/F_0, and the slopes are proportional to the spark volume. Even without endogenous buffers, about 20 pA of current is needed to produce a spherically symmetric spark having FWHM of 2 μm.

The spark amplitudes of actual sparks are expected to be larger if blurring were eliminated. To check if the calculated minimum current is valid, we simulated a spherically symmetric spark using a current of 2.4 pA, setting H_B to zero, and using values of k_D^+ and k_D^- that were 100 times larger than standard, to approximate an infinitely fast reaction. The FWHM of this simulated spark was 0.92 μm, which is close to the predicted value of 1.0 μm. The amplitude (F/F_0) of the unblurred spark was 12.1.

Effects of spark symmetry

In cardiac cells, sparks are often spatially asymmetric, being larger along the longitudinal, x, direction than in the transverse, y and presumably z, direction (Parker et al., 1996). The center curve (Fig. 3, *squares*) has been calculated for an asymmetric spark that has longitudinal FWHM of 2 μm and transverse (along y and z) FWHM of 1.5 μm. To produce such a spark with amplitude of 12 requires 10.7 pA. The top curve (*triangles*) gives the current for a spherical spark with FWHM of 2 μm. These plots show that the requisite current increases linearly with F/F_0, and the slope depends on the spark dimensions. In fact, the ratio of the slopes equals the ratio of the volumes of the sparks, where the volume is $V = (4\pi/3)(\lambda_{yz}/2)^2(\lambda_x/2)$. The volume of the asymmetric spark ($\lambda_x = 2.0$ μm, $\lambda_{yz} = 1.5$ μm) is 4.5 times the volume of the small spherically symmetric spark ($\lambda_x = 1.0$ μm, $\lambda_{yz} = 1.0$ μm) and the large spherical spark ($\lambda_x = 2.0$ μm, $\lambda_{yz} = 2.0$ μm) has 8 times the volume. To produce a spherical spark that has an FWHM of 2.0 μm, instead of 1.0 μm, requires eight times as much current, 18.96 pA. It is, therefore, not surprising that previous spark simulations (Smith et al., 1998; Izu et al., 1998; Jiang et al., 1999) that used Ca^{2+} release channel currents of ~2 pA produced sparks that had a spatial FWHM of only ~1 μm.

The requisite current in the presence of endogenous Ca^{2+} buffers

The current required to produce a spark of a given FWHM in the presence of endogenous Ca^{2+} buffers can be found by setting H_B (total concentration of free and bound buffer) to the desired value. Figure 4 A shows the required current to produce a spherical spark having FWHM $= 1.0$ μm (*circles*) and an ellipsoidal spark with dimensions ($\lambda_x = 2.0$ μm, $\lambda_{yz} = 1.5$ μm) (*squares*) when the endogenous buffer concentration was fixed to 123 μM (Berlin et al., 1994) and the total dye concentration varied. The current varies linearly with the free dye concentration, F_D, and, as before, the ratio of the slope of the lines equals the ratio of the volumes of the two sparks. As expected, much larger currents are required when endogenous buffers are present. For example, without endogenous buffers, 10.7 pA is needed to produce the asymmetric spark (marked with asterisk in Figure 3) but 37.7 pA is required when the endogenous
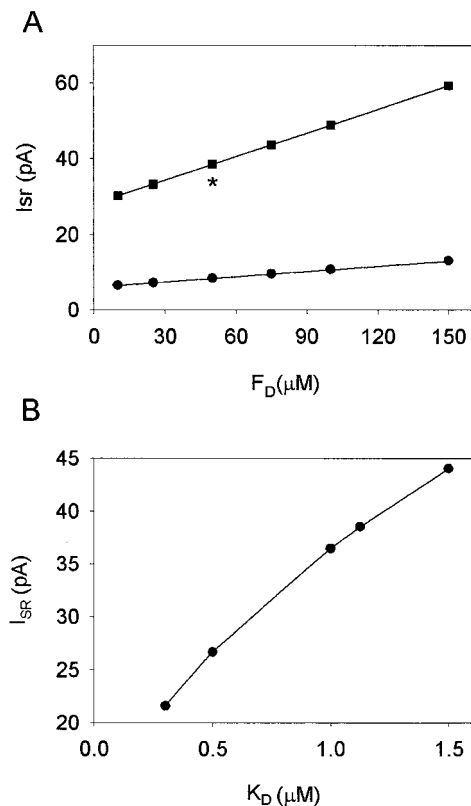
A

B

FIGURE 4 Current required to produce sparks of given spatial size. (A) Required current varies only slowly with the total dye concentration. A 10-fold increase in dye concentration only doubles the required current. Thus, small differences in dye loading should not materially affect FWHM measurements. Circles show the current for a spherical (1, 1, 1) spark and squares for an ellipsoidal (2, 1.5, 1.5) spark. (B) The current required to produce a (2, 1.5, 1.5) spark is strongly dependent on the dye's K_D. Other parameters used here are the standard values of the Smith buffer model.

buffer concentration is 123 μM (asterisk in Figure 4). I_{SR} is a rather weak function of the total dye concentration, however. Despite a 15-fold increase in H_D, the current had to only double to produce a spark of similar size and amplitude. Thus small, inevitable, differences in dye loading should not significantly affect the spark amplitude or FWHM. In contrast, I_{SR} is a fairly strong function of the dye's dissociation constant K_D, as seen in Fig. 4 B. A change in K_D from 500 nM to 1 μM, typical values used for calculating Ca^{2+} concentrations, changes I_{SR} by about 10 pA, a 36% increase.

Nonequilibrium models

Effect of dye saturation. The main result from the analysis above is that the currents required to produce Gaussian sparks that have the spatial extent of ~2 μm are much larger (~20–30 pA) than previously thought. In fact, however, large Ca^{2+} currents (e.g., 20 pA), will saturate a dye like fluo-3, so that G_D is no longer Gaussian, but platykurtic

(flat-topped). This will make the measured FWHM larger than predicted from the analysis above and reduce the requisite current. Figure 5 A shows unblurred spark profiles in a spherically symmetrical spark for various currents (5 ms in duration) using the Smith buffer model. The currents used were 1, 2, 5, 10, 20, 30, 40, and 50 pA. The amplitudes increase roughly proportionally to small currents, but reach an asymptotic value of $1 + K_D/C_o$ (= 12.25) (Fig. 5 B) at large currents. Figure 5 C shows that sparks do not attain an FWHM of 2 μm until I_{SR} is 50 pA (*circles*). Also plotted in this figure are the FWHM derived from backcalculation assuming chemical equilibrium and a Gaussian Ca^{2+}-bound dye profile (*squares*). Note that, for $I_{SR} < 20$ pA (where saturation is less severe) the backcalculated FWHM is larger than that from simulation, supporting our earlier conclusion that the equilibrium solution provides a lower bound for the current needed to produce a spark of a given spatial size. When dye saturation becomes severe ($I_{SR} > 20$ pA) and the Gaussian distribution no longer accurately describes the actual Ca^{2+}-bound dye distribution, the equilibrium estimate of the FWHM is lower than the simulation values. It should be noted that, in a linear system (approximating the case of no dye saturation), the FWHM is independent of the current because as the spark broadens the peak rises proportionally.

Difficulty in detecting platykurtic sparks. We mentioned earlier that the profiles of measured sparks could be well fit to a Gaussian distribution (Fig. 1 C). The spark profiles in Fig. 5 A, which have not been subjected to blurring by the microscope, are platykurtic when the currents are ≥30 pA so we might expect to see flat-topped sparks if saturation were occurring. To test whether we could detect such flat-topped sparks, we simulated optical blurring using the standard PSF (see Methods) and the PSF obtained from our "homebrew" confocal (Wier et al., 2000). The parameters of the homebrew PSF were (0.25, 0.25, 0.52) (in μm), which are better than the standard PSF. The standard PSF was chosen to account for the greater optical distortion likely to occur in the cell. The solid curve in Fig. 5 Da is the unblurred profile of the spark generated by $I_{SR} = 50$ pA. The spark profiles for blurring by the homebrew PSF is shown with the dashed curve and the profile using the standard PSF is given by the dot-dashed curve. Curves for the blurred sparks were displaced downward slightly to enhance clarity. The flat-top appearance of the spark is preserved with the homebrew PSF but becomes much less distinct with the standard PSF. At this time, we cannot deconvolve the effect of blurring for actual sparks because x–y–z scans of sparks cannot be collected within the time scale of sparks. But noise, not blurring, is probably more serious in masking dye saturation. Figure 5 Db shows that, after introducing noise (Izu et al., 1998) into the image, it becomes difficult to detect the signature flat-top of a saturated spark even with the superior PSF and we could fit the blurred, noisy spark profile with a Gaussian function.
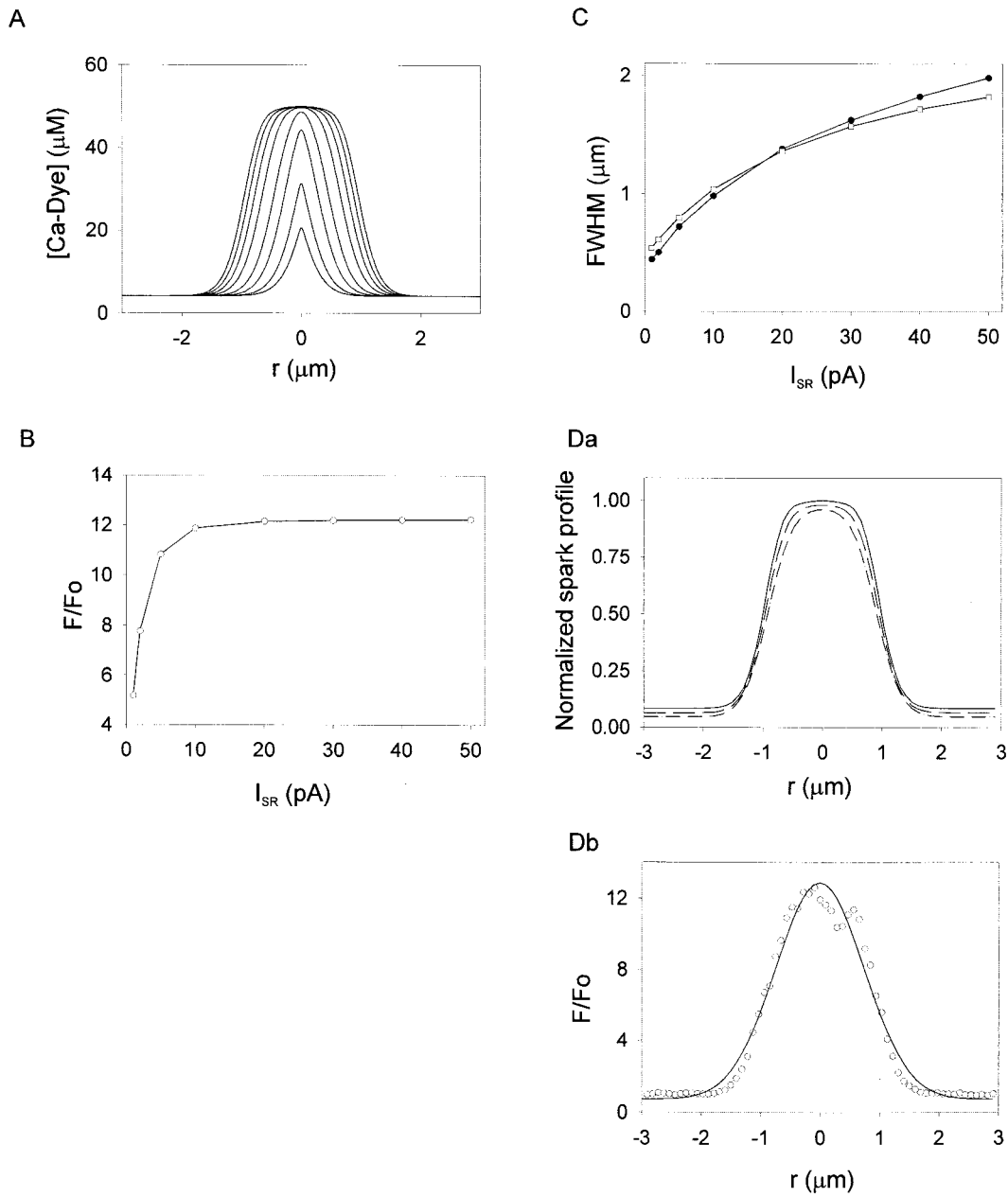
FIGURE 5 Spark properties for a range of release currents. (*A*) The unblurred Ca^{2+}-bound dye spatial profile along the *x*-axis at 5 ms, just before channel closing. Currents are 1, 2, 5, 10, 20, 30, 40, 50 pA. Spark amplitude for each current is given in Panel *B*. The amplitude increases approximately in proportion to the current when the currents are small but approaches the asymptote of 12.125 for currents above 10 pA. (*C*) The FWHM of the spherically symmetric sparks for standard dye kinetic parameters (*circles*) and infinite reaction rates (i.e., equilibrium distribution, *squares*). (*Da*) The normalized profiles of the unblurred (*solid line*) spark generated by 50-pA current and sparks blurred with either the homebrew PSF (*dashed*) or standard PSF (*dot-dashed*). The profiles for the blurred sparks were displaced downward slightly for clarity. After adding noise to the image blurred with the homebrew PSF, the characteristic flat-top profile is difficult to discern and the profile could be fit reasonably well with a Gaussian function (*Db*). Computation parameters are the standard Smith buffer model values.

Averaging multiple sparks would decrease the noise and might reveal dye saturation. To check this possibility, we averaged sparks (after normalization to the peak) collected with linescans at different positions (y, z) relative to the CRU at the origin. We used the homebrew blurring PSF to maximize the chance of detecting platykurtic sparks. Using linescans with coordinates ($y = 0.25 \ \mu$m $\times \ k$, $z = 0.25 \ \mu$m $\times \ k$; $k = 0, \ldots, 4$) yielded an average spark that was

almost perfectly Gaussian. These results indicate that the lack of observed platykurtic sparks does not indicate the absence of dye saturation.

Thus optical blurring eliminates one avenue for testing whether the dye is saturated. Other effects of microscope blurring on spark properties are considered later.

Asymmetric nonequilibrium cardiac Ca sparks. The last simulations showed that, when we take dye saturation into account, a 50-pA current is needed to generate a spherical 2-μm spark. Cardiac sparks are less than 2 μm in their transverse and axial dimensions, however (Parker et al., 1996). An asymmetric spark having dimensions $(\lambda_x, \lambda_y, \lambda_z) = (2, 1.5, 1.5)$ would have about the same spatial profile (that is the same FWHM) as a spherically symmetric $(2, 2, 2)$ spark, when viewed in a longitudinal linescan. Because the volume of the asymmetric spark is only 0.58 times that of the spherical spark, we predict that less current would be required to generate the asymmetric spark. To test this prediction, we generated spatially asymmetric sparks by reducing the diffusion coefficients of dye, bound dye, and Ca^{2+} to half standard values along the y and z directions from the x direction values (Parker et al., 1996). Figure 6 shows the variation in the longitudinal and transverse FWHM of the simulated sparks with current. A 20-pA current generated a spark with dimensions $(2, 1.4, 1.4)$. A slightly smaller spark having dimensions $(1.6, 1.2, 1.2)$ is generated with only 10 pA.

From these results, we conclude that cardiac sparks having a longitudinal FWHM of ~2 μm require about 20 pA of current for generation, assuming that the transverse and axial FWHM are ~1.5 μm. Because the volume of the spark scales with the current, relatively small changes in spark dimensions might reflect large changes in the underlying current.
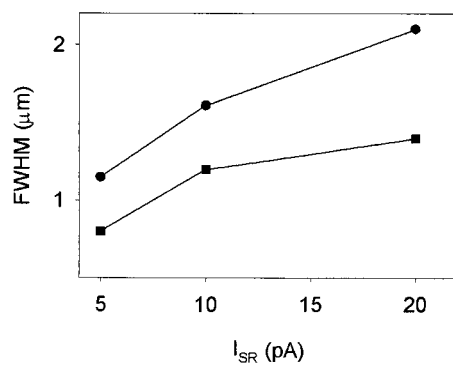

FIGURE 6 Dimensions of an ellipsoidal spark. Ellipsoidal sparks were generated using the Smith buffer model by reducing the transverse and axial diffusion coefficients of Ca^{2+}, F_D, and G_D by half from their longitudinal values of 0.3, 0.02, and 0.02 μm^2/ms, respectively. Circles indicate the longitudinal FWHM, and squares, the transverse FWHM. Note that only 20 pA of current is needed to produce a spark that has a longitudinal FWHM of 2 μm when the axial and transverse FWHM are 1.4 μm, but 50 pA is required to produce a spherical spark with FWHM = 2 μm (see Fig. 4 C).

Other factors that might increase the FWHM of cardiac Ca^{2+} sparks

We considered a number of schemes that might lead to spark sizes $\lambda_x \sim 2$ μm without invoking large currents. These schemes are superclusters of CRUs, a different buffer model, and assuming the existence of Ca^{2+}-releasing channels carrying small currents that surround the central large current CRU(s).

Superclusters of RyRs

In cardiac muscle, sparks might sometimes arise from the near-simultaneous release of calcium from a number of CRUs (Parker et al., 1996). It seemed possible that simultaneous release from multiple clusters of ryanodine receptors, or superclusters, could produce sparks that appear broader. First, sparks arising off the confocal linescan have larger FWHM, slowed kinetics, and decreased amplitude (Izu et al., 1998; Smith et al., 1998; Jiang et al., 1999). If the linescan passed perpendicularly through a planar lattice of release sites that fired simultaneously, then the linescan would pass, on average, between release sites. The resulting spark would be broad (because of its distance from the release site) but the amplitude would not be greatly decreased (because of summation from multiple release sites), producing a large FWHM. Additionally, when the CRUs are close together, buffer saturation can become prominent even when the currents from individual CRUs are relatively small. We simulated four release sites on the corners of a vertically oriented square having edges that measured either 0.4 or 0.8 μm, in rough approximation to 4 CRU surrounding a single myofibril at the z line. The smaller length is about the mean minimum distance between CRUs reported by Franzini-Armstrong et al. (1999). The larger length is about the mean distance between sparks measured in confocal linescans oriented transverse to the long axis of the cardiac cell (Parker et al., 1996). Table 2 shows λ_x and λ_y for sparks generated by 1 or 4 CRUs. The first three entries (labeled $1 \times I_{SR}$) are for a single CRU carrying current I_{SR}.

TABLE 2 Comparison of spark FWHM for different currents and CRU geometries

Configuration (pA)	L (μm)	λ_x (μm)	λ_y (μm)
1×5	—	1.2	0.8
1×10	—	1.6	1.2
1×20	—	2.0	1.4
4×2	0.4	1.2	1.2
4×5	0.4	2.0	1.6
4×10	0.8	2.0	2.1

The first three entries (labeled $1 \times I_{sr}$) are for a single CRU carrying current I_{SR}. The next three entries are for 4 CRUs on the corners of a square whose sides have length L. λ_x and λ_y are the FWHM of the spark measured longitudinally and transversely, respectively.

The linescan goes directly through the CRU. The next four entries (labeled $4 \times I_{SR}$) are for 4 CRUs on the corners of a square whose length is L, where each CRU carries current I_{SR}. The linescan for these simulations goes through the center of the square. When each CRU on the square carried 2 pA of current, the resulting spark had a longitudinal FWHM of just 1.2 μm. When the current through each CRU increased to 5 pA, the spark had a longitudinal FWHM of 2 μm, the same as a spark generated by a single CRU carrying 20 pA. Less dye saturation accounts for the fact that the $4 \times$ 2-pA spark is considerably smaller than a spark generated by a single CRU carrying 10 pA.

The results show that, when clusters of closely packed CRUs (spacing ~0.4–0.8 μm) fire simultaneously, the resulting spark would have a longitudinal FWHM ~ 2 μm although the current through each CRU is a modest 5–10 pA. However, a cluster of CRUs carrying smaller (~2 pA) currents still cannot generate sparks that have FWHM close to the observed values.

Ultrasmall channels

Lipp and Niggli (1999) observed highly localized (0.4-μm FWHM) tiny increases in fluorescence, which they suggested might be "quarks" (Lipp and Niggli, 1996). They estimated that these putative quarks are produced by currents only $\frac{1}{40}$–$\frac{1}{20}$ of those that produce a typical spark. Moreover, they occur away from the site of origin of the spark. In a preliminary model of Ca²⁺ waves, we found it necessary to intersperse small Ca²⁺ release channels carrying ~0.1 pA between channels carrying 2 pA to get Ca²⁺ wave propagation that matched experimental observations (Izu et al., 1999). Here we examined whether Ca²⁺ release from ultrasmall current channels surrounding a central channel carrying 2 pA would generate a spark that had an FWHM of ~2 μm. To test this, we placed the 2-pA channel at the center of a 2-dimensional square lattice having lattice period of 0.25 μm. (See Izu et al., 2001 for conversion of current to a flux appropriate for 2-dimensional systems.). Ultrasmall current channels carrying 0.1 pA were placed at each lattice site. To simulate Ca²⁺-induced Ca²⁺-release, these ultrasmall channels began to release Ca²⁺ when the ambient Ca²⁺ concentration reached about 500 nM. Within 1 ms after the central channel opened the adjacent 0.1 pA channels started releasing Ca²⁺. However, the contribution of the 0.1 pA channels to elevating the fluorescence (G_F) was almost completely masked by the fluorescence increase due to the much larger central channel. Thus, it is unlikely that if quarks exist that Ca²⁺ release from them is responsible for generating sparks with FWHM ~ 2 μm.

Possible protein-dye interactions

We showed above that the spark FWHM increases only slowly with increasing current because the broadening of

the G_D distribution is largely offset by the increase in peak. In skeletal muscle, a similar problem has been noted; model Ca²⁺ transients rise more rapidly at the release site and more slowly away from the release site than do recorded ones, making the model Ca²⁺ transients smaller in spatial spread (Hollingworth et al., 1999). This problem was ameliorated by considering possible protein–dye interactions, as described earlier (Harkins et al., 1993). The Harkins buffer model allows binding of dye (*D*) to protein, forming *PD*, the binding of Ca-bound fluo-3 (*CaD*) to protein, forming *CaPD*, as well as the binding of Ca²⁺ to *PD*, also forming *CaPD*. *PD* has a lower affinity for Ca than free dye (*D*) (1.92 and 0.51 μM, respectively). Ca-bound fluo-3 (*CaD*) has a lower affinity for protein than free fluo-3 (*D*) (1378 and 366 μM, respectively). Thus, when Ca²⁺ is released, *CaD* rises and the loss of *D* is compensated by the unbinding of dye from its protein-bound form. The dynamic increase of *D* and the greater diffusivity of *CaD* over *CaPD* should decrease the amplitude and broaden the spark.

Numerical simulations of the Harkins model required a mesh spacing finer than 0.1 μm used in the 3D simulations of the Smith model. This requirement made the computations prohibitively long (>24 hrs per ms of simulation time), so all results were obtained assuming spherical symmetry. *Ca* and *CaD* were assumed to be mobile with diffusion coefficients of 0.3 and 0.09 μm²/ms, respectively. Figure 7 *A* shows the FWHM of the sparks generated from the Harkins (*squares*) and Smith (*circles*) buffer models. The FWHM without and with blurring (see below) are given by the open and solid symbols, respectively. Sparks from the Harkins buffer model have a larger FWHM than those from the Smith buffer model, which is in accord with our intuitive predictions. However, the relatively large currents (~40 pA) are still required to generate sparks having FWHM ~ 2 μm in the Harkins buffer model.

The most striking difference between the Smith and Harkins models is the spark amplitude shown in Fig. 7 *B*. The amplitude of sparks from the Smith model is about twice those from the Harkins model. The difference arises from the different dye dissociation constants in the two models. For any dye, the maximum achievable amplitude is $1 + K_D/C_o$. For the protein-free dye in the Harkins model, $K_{D1} = 0.51$ μM, so the maximum amplitude is 6.1. The protein-bound dye has K_{D2} of 1.92 μM so the maximum amplitude is 20.2. However, because most of the Ca-bound dye is in the protein-free form (*CaD*), the peak amplitude is close to 6.1. In the Smith model, $K_D = 1.125$ μM, and the peak amplitude for large currents is about the maximum achievable of 12.25.

Blurring by the confocal microscope

Earlier, we have seen that optical blurring by the confocal microscope made the detection of platykurtic sparks difficult. We now consider other effects that blurring has on
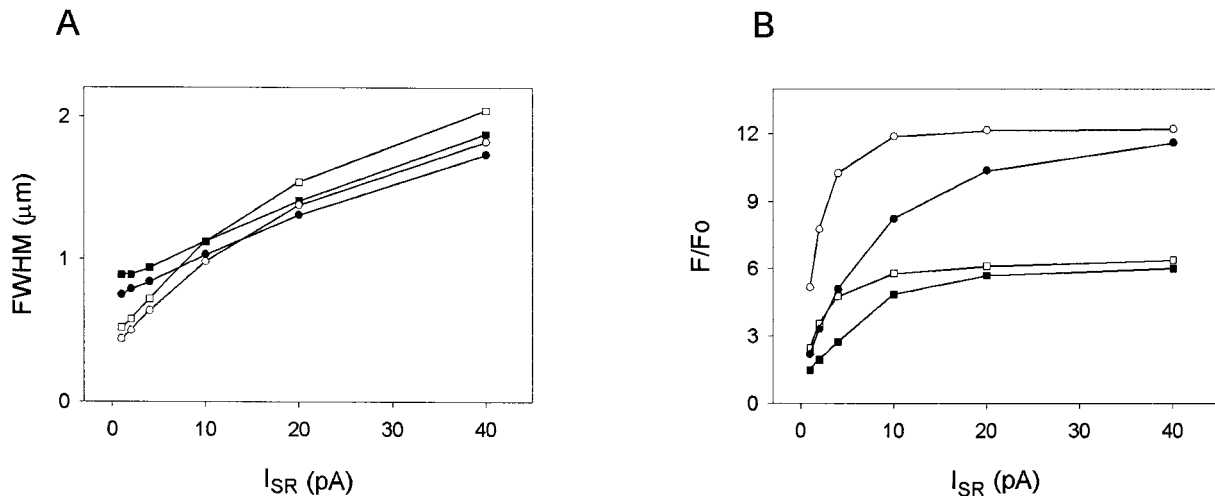
A

B

FIGURE 7 Comparison of sparks generated by the Smith and Harkins buffer models. (*A*) The FWHM of spherical sparks for the Smith (*circles*) and Harkins (*squares*) buffer models. The empty symbols indicate no blurring, and filled symbols show the values obtained with optical blurring. For the same current, the Harkins model produces slightly larger sparks. The chief difference between the two models lies in the spark amplitudes shown in Panel *B*. The spark amplitudes for the Harkins model are about half of those in the Smith model. See text for explanation for the differences in blurred and unblurred values for the FWHM and amplitude. Simulation parameters for Harkins buffer model (Hollingworth et al., 1999): on- and off-rate constants of Ca^{2+} with fluo-2 were, 3.5×10^8 per μM/s and 179/s for protein-free fluo-3 and 2.25×10^7 per μM/s and 43/s for protein-bound fluo-3. On- and off-rate constants for the reaction of protein with fluo-3 were 1×10^7 per μM/s and 3.67×10^3 per s for Ca^{2+}-free fluo-3 and 1×10^7 per μM/s and 1.38×10^3 per s for Ca^{2+}-bound-fluo-3. $D_{Cx} = 0.3$ μm^2/ms, $D_{Dx} = 0.09$ μm^2/ms, total protein = 123 μM, Ca^{2+}-free dye = 50 μM (at rest). SR-pump parameters are the same as in Smith buffer model.

spark properties, particularly on the possible importance of this factor in producing sparks with large FWHM.

From Eq. B3, we see that the FWHM of the blurred spark is $FWHM_i = \sqrt{FWHM_m^2 + FWHM_o^2}$, where the subscripts i, m, and o refer to the image, microscope, and object; this equation holds exactly when the object and blurring kernel are described by Gaussian functions. Thus, when the spark is spatially small, the FWHM of the blurred spark is determined to a large extend by the microscope's FWHM. Accordingly, when the currents are small, the unblurred sparks are narrower than the blurred sparks. This is seen in Fig. 7 *A*, where the spark FWHM for the blurred image (*solid symbols*) lie above those for the unblurred image (*open symbols*) for currents <10 pA. The ratio of the spark amplitude of the blurred to unblurred spark image scales as $FWHM_o/FWHM_m$ when this ratio is small (Eq. B3), and approaches 1 when the object is large. This behavior is illustrated in Fig. 7 *B* where the amplitude of the blurred spark (*closed symbols*) lies below the unblurred amplitude. Thus, blurring by the microscope will distort sparks generated by small currents, making them appear wider and dimmer. However, as the sparks become larger, the PSF of the microscope figures less prominently in determining the measured FWHM of the spark. When the current is 10 pA, the FWHM of the blurred and unblurred sparks are almost identical.

However, when the currents are large and dye saturation significant, the unblurred spark profile is platykurtic. As seen earlier, blurring rounds out the flat top giving the spark

a more Gaussian profile. Consequently, the FWHM of the blurred spark is narrower than the unblurred spark (Fig. 5 *Da*). Thus, in Fig. 7 *A* the FWHM of the unblurred sparks exceed those of the blurred sparks for currents >10 pA. The difference is fairly small, however, amounting to <5% for the Smith model and <10% for the Harkins model. Thus, blurring by the microscope should have minimal effect on the measured FWHM and amplitude of sparks with FWHM ~ 1 μm. Nevertheless, blurring is not benign because it makes detection of saturated sparks difficult.

Temporal properties of sparks for long channel openings

Cardiac Ca^{2+} sparks typically reach their peak in 5–10 ms (Cheng et al., 1993) then begin to decay immediately. The fluorescence of some sparks, however, remain elevated for long times (tens of ms) in the presence of ryanodine (Cheng et al., 1993), or spontaneously (Parker and Wier, 1997), or when inactivation is blocked (Xiao et al., 1997). These long-lived sparks presumably reflect long openings of the RyRs. The fluorescence of these long-lived sparks rises abruptly to a peak, and then stays there or falls rapidly to a plateau. We compared the temporal features of sparks generated by 2-pA and 20-pA currents that flowed for 25 ms, much longer than the standard 5-ms open time. For the 2-pA channel, the fluorescence rises gradually and continuously throughout the time the CRU stays open (Fig. 8 *A*). The spark generated by 20-pA current behaves differently (Fig. 8 *B*). The fluorescence does not rise continuously during the
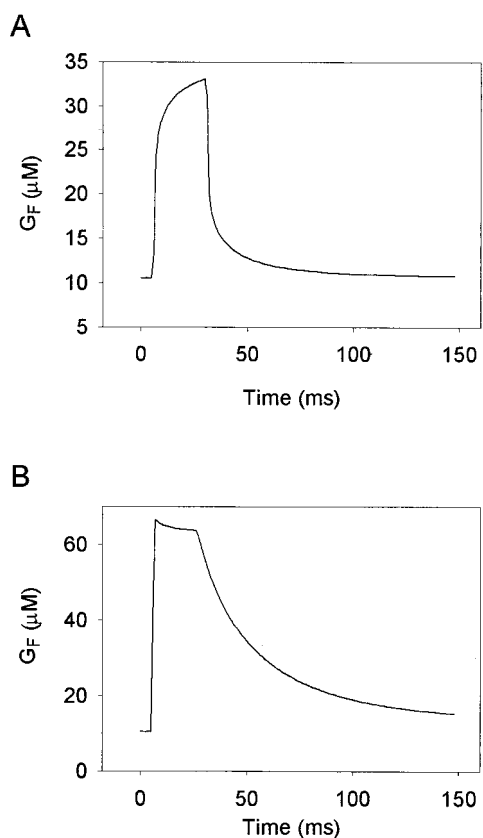
FIGURE 8 Comparison of temporal properties of sparks generated by small and large currents for long channel opening. The temporal profiles of sparks generated by (A) small (2 pA) or (B) large (20 pA) differ significantly. Both channels were open for 25 ms. For small currents, the fluorescence rises continuously throughout the time the channel is open. By contrast, when the current is large the fluorescence rises rapidly, overshoots, then plateaus. The overshoot occurs in the Harkins buffer model but not in the Smith buffer model.

CRU opening but instead rises rapidly, "overshoots" slightly, then plateaus. The absence of a continuously rising fluorescence signal in experimentally measured sparks with long channel openings may indicate dye saturation and large underlying currents. We note that the overshoot and plateau in the simulated sparks is caused by the unloading of the Ca^{2+} by the protein-bound dye, *CaPD*, to regenerate *PD*. In all simulations, the differences between the peak and plateau level were small, but, in some experimentally measured sparks, there can be substantial differences between peak and plateau fluorescence levels (Xiao et al., 1997). In actual sparks, the overshoot and drop to a lower plateau may reflect a more complicated mechanism such as the closing of a few channels in the CRU.

DISCUSSION

In summary, we have presented a series of estimates of the total current through a CRU needed to produce a spark of

spatial dimensions (λ_x, λ_y, λ_z), where the λ are the FWHM (in μm) along the ventricular myocyte's longitudinal axis, transverse axis, and the microscope's z-axis. The first estimate assumed all buffer reactions were in equilibrium and that the spatial distribution of the Ca^{2+}-bound fluo-3 was Gaussian. This estimate established a lower bound for the required current in the absence of fluo-3 saturation. A spherical spark with FWHM of 2 μm requires ~20 pA, even without endogenous buffers. The required current scales linearly with the spark volume, so only 10.7 pA is required to produce an ellipsoidal spark with dimensions (2, 1.5, 1.5). To produce the same sized spark in the presence of 123 μM endogenous buffer however, requires ~38 pA.

Large currents however, cause significant dye saturation, so the computed Ca^{2+}-bound fluo-3 spatial profile is not Gaussian, but platykurtic. The FWHM for the platykurtic distribution is significantly larger, given the same current. By taking possible dye saturation into account, we found that 20 pA was needed to produce a (2, 1.4, 1.4) spark. A 10-pA current will generate a spark with dimensions (1.6, 1.2, 1.2). This is about half the current estimated when the spark had a Gaussian profile.

Currents of this magnitude (~10–20 pA) are close to the 16–20 pA estimate that Rios et al. (1999) made for currents underlying sparks in skeletal muscle. These large currents produce Ca–dye distributions that are platykurtic. The fact that the largest Ca^{2+} sparks were not platykurtic seems to argue against the notion that sparks arise from large currents from a small source region. However, optical blurring and noise makes detecting the flat-top saturation signature of even the widest spark (generated by 50 pA) difficult (Fig. 5, *Da* and *Db*). Hence, the absence of flat-topped sparks cannot be used to rule out the possibility that large currents underlie sparks. This is important, because an alternate way of generating spatially broad sparks without using large currents is to lengthen the size of the source along the long axis of the cell (DiGregorio et al., 1999; Gonzalez et al., 2000). This possibility is favored by Gonzalez et al. (2000) for generating sparks in skeletal muscle because it appears that dye saturation does not occur there. As Gonzalez et al. point out, however, such an extended source requires RyRs to lie outside the plane of the z-line.

For currents $\geq$5 pA the computed spark amplitudes (F/F_0) are large, ~6 for Harkins buffer model, or ~12 for Smith buffer model. We and others (Cheng et al., 1993, 1999; López-López et al., 1995) measured sparks with amplitudes of F/F_0 of ~2–3, considerably smaller than predicted from the model. Recently, however, Shirokova et al. (1999) have measured large amplitude (~9) sparks in developing mouse skeletal muscle. We now also measure sparks with large amplitude (~6) occasionally (Fig. 1 and Wier et al., 2000).

We attribute the measurement of large amplitude sparks using our custom confocal microscope (Wier et al., 2000),

in part, to the better optical resolution and differences in photon detection compared to our BioRad 600. We measured a population of sparks in cells on the same coverslip using the homebrew confocal and the BioRad within a few minutes of each other. In this way, differences in spark characteristics due to different animals, loading conditions, or cell isolation are minimized or eliminated (C. Lamont, J. Mauban, and W. G. Wier, unpublished observations). The mean spark amplitude was larger in the population measured with the custom confocal microscope than in the BioRad (3.1 versus 2.0, $p < 0.001$ using Student's t-test). The amplitudes of the largest sparks were also larger when measured with the custom confocal microscope than with the BioRad (8.5 versus 4.2). From the optical standpoint, any reasonably aligned confocal microscope should record about the same spark amplitude and FWHM for the largest sparks, because the FWHM of a large spark (~ 2 μm) is much larger than the lateral FWHM of the PSF of a typical microscope objective used for measuring sparks (<0.5 μm). For example, the spark amplitude and FWHM for the blurred and unblurred spark are similar when the underlying current is large, ~ 40 pA (Fig. 7). Thus, differences in photon detection between the homebrew confocal and the BioRad is likely to be important in accounting for the differences in spark amplitudes measured in these two systems.

The magnitude of I_{SR} is not the sole determinant of the spark amplitude. The K_d of the dye strongly affects amplitude. The spark amplitude is smaller in the Harkins than in the Smith buffer model for the same current because, in the former, most of the Ca-bound dye is in the free (not protein-bound) form, which has a K_d of 0.51 μM. In the Smith buffer model, $K_d = 1.125$ μM. The dye's K_d also strongly influences the spark FWHM (Fig. 4 B). Hence, decreasing K_d decreases the spark amplitude while increasing the FWHM for the same current. Another important determinant of the spark amplitude is the resting Ca^{2+} level. Large currents generate large spark amplitudes, but large amplitudes do not necessarily imply large underlying currents. We cannot exclude the possibility that subtle changes in dye loading or cell isolation might affect the dye K_d, resting Ca^{2+} level, or SR load that affects I_{SR}, which may be responsible, at least in part, for the larger spark amplitudes we now measure.

We considered several factors that might produce sparks with FWHM ~ 2 μm without using large currents. With protein–dye interactions allowed (Harkins et al., 1993), the spark FWHM increased slightly but not enough to obviate the need for large (~ 20 pA) currents. Blurring of sparks by the microscope increased the apparent FWHM of small (~ 0.5 μm) sparks but did not materially affect the FWHM of larger (~ 1 μm) sparks for typical microscope resolution parameters.

Our analysis suggests that sparks are likely to originate from either a single CRU carrying ~ 20 pA of current or clusters of closely spaced (~ 0.4–0.8 μm) CRUs carrying about 5–10 pA. Taking a recent estimate of the single ryanodine receptor current of ~ 0.6 pA, sparks may thus represent the concerted opening of ~ 10–30 ryanodine receptors.

APPENDIX A

We prove that G_D^∞ has a larger FWHM than G_D. Let $\bar{x}_\infty$ and $\bar{x}$ be the half-amplitude points (along the x-direction) for G_D^∞ and G_D. Then we will show that $\bar{x}_\infty > \bar{x}$. Because of the assumed symmetric form of the Ca-bound dye, similar results hold for the y and z directions. Thus, we drop the y and z exponentials and let

$$G_D^\infty(x) = G_D^{\infty,p} \exp[-x^2/(2\sigma_\infty^2)]$$

and (A1)

$$G_D(x) = G_D^p \exp[-x^2/(2\sigma^2)].$$

We show $\bar{x}_\infty > \bar{x}$ by contradiction. Suppose $\bar{x}_\infty \le \bar{x}$, then we can show there is an x^* such that $G_D^\infty(x^*) < G_D(x^*)$. Because $\bar{x} = \sigma\sqrt{2\ln(2)}$, $\sigma_\infty < \sigma$. Setting $G_D^\infty(x) = G_D(x)$ and solving for x gives

$$x^2\left(\frac{1}{2\sigma^2} - \frac{1}{2\sigma_\infty^2}\right) = \ln(G_D^p/G_D^{\infty,p}). \qquad (A2)$$

Because the right-hand side is less than 0 and because, by assumption, $\sigma > \sigma_\infty$, the difference on the left-hand side is negative, so the equation has the real solution x^*. The slopes of G_D^∞ and G_D at x^* are $-\alpha x^*/\sigma_\infty^2$ and $-\alpha x^*/\sigma^2$, respectively, where $\alpha = G_D^\infty(x^*) = G_D(x^*)$. Supposing $x^* > 0$, clearly, G_D^∞ has a steeper slope than G_D at x^*, so $G_D^\infty(x) < G_D(x)$ in a neighborhood of $x > x^*$ (in fact, for all $x > x^*$), thus contradicting the assumption that $G_D^\infty(x) \ge G_D(x)$ for all x. (The argument is the same for $x^* < 0$ but with inequality signs reversed.)

APPENDIX B

To understand the effect of the blurring kernel on the spark FWHM, it is useful to have an exactly solvable example. Let $K(x)$ be the normalized Gaussian blurring kernel,

$$K(x) = \frac{1}{p\sqrt{2\pi}} \exp\left(\frac{-x^2}{2p^2}\right), \qquad (B1)$$

and let $f(x)$ be a Gaussian object,

$$f(x) = A \exp\left(\frac{-x^2}{2q^2}\right). \qquad (B2)$$

The image $I(x)$ is given by the convolution of K and f,

$$I(x) = \frac{Aq}{\sqrt{p^2 + q^2}} \exp\left(\frac{-x^2}{2(p^2 + q^2)}\right)$$

$$= \frac{A\alpha}{\sqrt{1 + \alpha^2}} \exp\left(\frac{-x^2}{2p^2(1 + \alpha^2)}\right), \quad q = \alpha p. \quad (B3)$$

The relationship between the microscope's FWHM of the PSF, FWHM(m), and p is FWHM(m) = $\sqrt{8\ln(2)}p$ and likewise for the object. When the object FWHM is much smaller than the microscope's ($\alpha \ll 1$), then Eq. B3 becomes $I(x) \rightarrow A\alpha \exp(-x^2/(2p^2))$, showing that the object becomes dim and has the FWHM of the microscope's PSF. Conversely, when the

object is large relative to the microscope's FWHM(m) ($\alpha \gg 1$) then $I(x) \to A \exp(-x^2/(2q^2))$, which is identical to the object.

APPENDIX C

We consider the 3D linear diffusion problem,

$$\frac{\partial C}{\partial t} = \nabla \cdot (D_c \nabla C), \tag{C1}$$

where the right-hand side is given by Eq. 6 and satisfying the boundary condition $C(r, t) \to 0$ as $r \to \infty$, where r is the Euclidean distance. For the initial condition in which M moles of Ca²⁺ is deposited in an infinitesimal volume at the origin at $t = 0$, the solution to Eq. C1 can be readily verified to be

$$C(x, y, z, t)$$

$$= \frac{M}{\sqrt{D_x D_y D_z (4\pi t^3)}} \exp\left(\frac{-x^2}{4D_x t}\right) \cdot \exp\left(\frac{-y^2}{4D_y t}\right) \cdot \exp\left(\frac{-z^2}{4D_z t}\right)$$

$$\equiv MG(x, y, z, t). \tag{C2}$$

If, instead, of all M moles of Ca²⁺ being deposited instantly at the origin at $t = 0$, Ca²⁺ is introduced at a rate of q mol/s (as with a CRU) at the origin, then $C(x, y, z, t)$ is obtained from convolving G with q and is

$$C(x, y, z, t) = \frac{q}{\sqrt{(4\pi)^3 D_x D_y D_z}} \frac{\sqrt{\pi}}{\sqrt{\dfrac{x^2}{4D_x} + \dfrac{y^2}{4D_y} + \dfrac{z^2}{4D_z}}}$$

$$\times \mathrm{erfc}\left(\frac{\sqrt{\dfrac{x^2}{4D_x} + \dfrac{y^2}{4D_y} + \dfrac{z^2}{4D_z}}}{\sqrt{t}}\right). \tag{C3}$$

We used this closed form solution, Eq. C3, to gauge the accuracy of our numerical solution.

REFERENCES

Backx, P. H., P. P. De Tombe, J. H. K. Van Deen, B. J. M. Mulder, H. E. D. J. ter Keurs. 1989. A model of propagating calcium-induced calcium release mediated by calcium diffusion. *J. Gen. Physiol.* 93: 963–977.

Balke, C. W., T. M. Egan, and W. G. Wier. 1994. Processes that remove calcium from the cytoplasm during excitation–contraction coupling in intact rat heart cells. *J. Physiol.* 474:447–462.

Baylor, S. M., and S. Hollingworth. 1998. Model of sarcomeric Ca²⁺ movements, including ATP Ca²⁺ binding and diffusion, during activation of frog skeletal muscle. *J. Gen. Physiol.* 112:297–316.

Berlin, J. R., J. W. M. Bassani, and D. M. Bers. 1994. Intrinsic cytosolic calcium buffering properties of single rat cardiac myocytes. *Biophys. J.* 67:1775–1787.

Blatter, L. A., J. Hüser, and E. Ríos. 1997. Sarcoplasmic reticulum Ca²⁺ release flux underlying Ca²⁺ sparks in cardiac muscle. *Proc. Natl. Acad. Sci. USA.* 94:4176–4181.

Blatter, L. A., and W. G. Wier. 1990. Intracellular diffusion, binding, and compartmentalization of the fluorescent calcium indicators indo-1 and fura-2. *Biophys. J.* 58:1491–1499.

Cheng, H., W. J. Lederer, and M. B. Cannell. 1993. Calcium sparks: elementary events underlying excitation–contraction coupling in heart muscle. *Science.* 262:740–744.

Cheng, H., L.-S. Song, N. Shirokova, A. Gonzalez, E. Lakatta, E. Ríos, and M. Stern. 1999. Amplitude distribution of calcium sparks in confocal images: theory and studies with an automatic detection method. *Biophys. J.* 76:606–617.

Cheng, H., M. R. Lederer, W. J. Lederer, and M. B. Cannell. 1996a. Calcium sparks and [Ca²⁺]ᵢ waves in cardiac myocytes. *Am. J. Physiol. Cell Physiol.* 270:C148–C159.

Cheng, H., M. R. Lederer, R.-P. Xiao, A. M. Gomez, Y.-Y. Zhou, B. Ziman, H. Spurgeon, E. G. Lakatta, and W. J. Lederer. 1996b. Excitation–contraction coupling in heart: new insights from Ca²⁺ sparks. *Cell Calcium.* 20:129–140.

Crank, J. 1975. The Mathematics of Diffusion. 2nd ed. Oxford University Press, London, U.K. 89.

DiGregorio, D. A., A. Peskoff, and J. L. Vergara. 1999. The dimensions of presynaptic calcium entry sites estimated from measured calcium domains in cultured neuromuscular junctions. *Biophys. J.* 76:A21.

Franzini-Armstrong, C., F. Protasi, and V. Ramesh. 1999. Shape, size, and distribution of Ca²⁺ release units and couplons in skeletal and cardiac muscles. *Biophys. J.* 77:1528–1539.

Gonzalez, A., W. G. Kirsch, N. Shirokova, G. Pizarro, M. D. Stern, and E. Ríos. 2000. The spark and its ember. Separately gated local components of Ca²⁺ release in skeletal muscle. *J. Gen. Physiol.* 115:139–157.

Harkins, A. B., N. Kurebayashi, and S. M. Baylor. 1993. Resting myoplasmic free calcium in frog skeletal muscle fibers estimated with fluo-3. *Biophys. J.* 65:865–881.

Hollingworth, S., C. Soeller, S. M. Baylor, and M. B. Cannell. 1999. In skeletal muscle fibers, a rise in myoplasmic calcium appears to speed the diffusion of fluo-3 by perturbing the equilibrium between protein-free and protein-bound indicator. *J. Gen. Physiol.* 114:11A.

Izu, L. T., W. G. Wier, and C. W. Balke. 1998. Theoretical analysis of the Ca²⁺ spark amplitude distribution. *Biophys. J.* 75:1144–1162.

Izu, L. T., W. G. Wier, and C. W. Balke. 1999. Evolution of Ca²⁺ waves from stochastic Ca²⁺ sparks on rectangular lattices. *Biophys. J.* 76: A397.

Izu, L. T., W. G. Wier, and C. W. Balke. 2001. Evolution of cardiac Ca²⁺ waves from stochastic Ca²⁺ sparks. *Biophys. J.* 80:88–102.

Jiang, Y.-H., M. G. Klein, and M. F. Schneider. 1999. Numerical simulation of Ca²⁺ "sparks" in skeletal muscle. *Biophys. J.* 77:2333–2357.

Kahaner, D., C. Moler, and S. Nash. 1988. Numerical Methods and Software. Prentice Hall, Englewood Cliffs, NJ. 176–179.

Lacampagne, A., C. W. Ward, M. G. Klein, and M. F. Schneider. 1999. Time course of individual Ca²⁺ sparks in frog skeletal muscle recorded at high time resolution. *J. Gen. Physiol.* 113:187–198.

Lipp, P., and E. Niggli. 1996. Submicroscopic calcium signals as fundamental events of excitation–contraction coupling in guinea-pig cardiac myocytes. *J. Physiol.* 492:31–38.

Lipp, P., and E. Niggli. 1999. Fundamental calcium release events revealed by two-photon excitation photolysis of caged calcium in guinea-pig cardiac myocytes. *J. Physiol.* 508:801–809.

López-López, J. R., P. S. Shacklock, C. W. Balke, and W. G. Wier. 1995. Local calcium transients triggered by single L-type calcium channel currents in cardiac cells. *Science.* 268:1042–1045.

Lukyanenko, V., I. Györke, and S. Györke. 1996. Regulation of calcium release by calcium inside the sarcoplasmic reticulum in ventricular myocytes. *Pflügers Arch. Eur. J. Physiol.* 432:1047–1054.

Lukyanenko, V., S. Subramanian, I. Györke, T. Wiesner, and S. Györke. 1999. The role of luminal Ca²⁺ in the generation of Ca²⁺ waves in rat ventricular myocytes. *J. Physiol.* 518:173–186.

Parker, I., W.-J. Zang, and W. G. Wier. 1996. Ca^{2+} sparks involving multiple Ca^{2+} release sites along z-lines in rat heart cells. *J. Physiol.* 497:31–38.

Parker, I., and W. G. Wier. 1997. Variability in frequency and characteristics of Ca^{2+} sparks at different release sites in rat ventricular myocytes. *J. Physiol.* 505:337–344.

Ríos, E., M. D. Stern, A. González, G. Pizzarro, and N. Shirokova. 1999. Calcium release flux underlying Ca^{2+} sparks of frog skeletal muscle. *J. Gen. Physiol.* 114:31–48.

Rousseau, E., and G. Meissner. 1989. Single cardiac sarcoplasmic reticulum Ca^{2+} release channel: activation by caffeine. *Am. J. Physiol. Heart Circ. Physiol.* 256:H328–H333.

Shirokova, N., R. Shirokov, D. Rossi, A. González, W. G. Kirsch, J. García, V. Sorrentino, and E. Ríos. 1999. Spatially segregated control of Ca^{2+} release in developing skeletal muscle of mice. *J. Physiol.* 521:483–495.

Smith, G. D., J. E. Keizer, M. D. Stern, W. J. Lederer, and H. Cheng. 1998. A simple numerical model of calcium spark formation and detection in cardiac myocytes. *Biophys. J.* 75:15–32.

Wier, W. G., C. W. Balke, J. A. Michael, and J. R. H. Mauban. 2000. A custom confocal and two-photon digital laser scanning microscope. *Am. J. Physiol. Heart Circ. Physiol.* 278:H51–H56.

Wier, W. G., H. E. D. J. ter Keurs, E. Marban, W. D. Gao, and C. W. Balke. 1997. Ca^{2+} "sparks" and waves in intact ventricular muscle resolved by confocal imaging. *Circ. Res.* 81:462–469.

Xiao, R.-P., H. H. Valdivia, K. Bogdanov, C. Valdivia, E. Lakatta, and H. Cheng. 1997. The immunophilin FK506-binding protein modulates Ca^{2+} release channel closure in rat heart. *J. Physiol.* 500:343–354.